PAPER

Check for updates

High photocatalytic performance of ZnGa2O4/Ga2O3 double-shell hollow sphere structures prepared *via* a one-step hydrothermal method†

Zeyu Yang,[a] Jizhou Yang[b] and Haibo Fan [iD] *[b]

In this study, photocatalytic degradation of rhodamine B (RhB) using one-step hydrothermally prepared ZnGa2O4/Ga2O3 heterojunctions with double-shell hollow sphere structures was investigated. It was found that this structure greatly improved the photocatalytic performance through the formation of an S-scheme heterojunction at the interface between ZnGa2O4 and Ga2O3. By optimizing the feed ratio, a maximum RhB degradation rate of 0.1133 min^{-1} was obtained, which was nearly 2 times higher than that of the Ga2O3 monomer photocatalyst, 5 times higher than that of the ZnGa2O4 monomer photocatalyst, and 96 times higher than the RhB self-degradation rate. Capture experiments showed that h$^+$ played a key role in the efficient decomposition of RhB reactive groups. This study provides a new idea and a simple preparation method for the novel ZnGa2O4/Ga2O3 S-scheme heterojunctions for efficient photocatalytic degradation of organic pollutants.

1. Introduction

This study presents a simple hydrothermal method for preparing ZnGa2O4/Ga2O3 heterojunctions for high-efficiency photocatalysis. As environmental pollution becomes increasingly severe, traditional methods such as physical adsorption and biodegradation can remove some pollutants, but they could also introduce new impurities. In the absence of an efficient pollutant removal strategy, environmental pollution will continue to pose significant threats to human health.[1–3] Traditional methods require substantial investments in manpower, materials and financial resources. Traditional decontamination methods are not only time-consuming,[4,5] in the current environment, the rate of repair is much lower than the rate of pollution.[6–8] Accordingly, traditional methods are obviously not suitable for the current context. Modern society demands environmental technologies that are more efficient, non-toxic and harmless. This has led to the emergence of semiconductor photocatalysis technology. Semiconductor photocatalysis relies on semiconductors and sunlight, using semiconductors as catalysts. It consumes only clean solar energy and relies on the REDOX ability of semiconductors to oxidize organic pollutants into non-toxic and harmless substances without producing secondary pollution, making it a promising technology.[9–12] Some common semiconductors have attracted public attention. TiO2,[13–15] Ga2O3[16–18] and other third- and fourth-generation semiconductors have been extensively studied in the field of photocatalysis because of their strong photocatalytic degradation rates.

The most important selection criteria for semiconductor photocatalysts are the conduction band (CB) and valence band (VB) positions of the semiconductor, which determine the REDOX capacity of the semiconductor. Among all the semiconductors, ZnGa2O4 is a good semiconductor material because of its unique crystal structure and wide band gap.[19] Sun's work demonstrated that ZnGa2O4 can be superior to P25 (TiO2) for photocatalytic activity in some cases.[20] Inoue proved that the 4s4p orbital of Ga and the 4s4p orbital of Zn could increase the dispersion in the conduction band, which are advantageous for the decrease in the band gap and increase in the activity of the photocatalyst.[21] The strong interaction between Zn and Ga is observed in ZnGa2O4. Notably, Zn^{2+} in ZnGa2O4 belongs to the d^{10} structure, so it has good chemical and thermal stability. Both Zn and Ga have a small effective electron mass in the compound, which accelerates the migration of ZnGa2O4 photogenerated carriers to the surface, making them more favorable for photocatalysis.

For a semiconductor, an extremely wide band gap can make the semiconductor have a strong REDOX ability, but it can also make the semiconductor material's absorption threshold of light low and can only absorb ultraviolet light. The recombination of photoelectron hole pairs in semiconductors with direct band gaps limits the photocatalytic performance.[22] To solve the

[a] *School of Microelectronics, Xidian University, Xi'an 710071, China.*
 E-mail: hbfan@nwu.edu.cn
[b] *School of Physics, Northwest University, Xi'an 710127, China*
† Electronic supplementary information (ESI) available. See DOI: **https://doi.org/10.1039/d5ma00179j**

problem of rapid photogenerated carrier recombination, semiconductors are usually constructed using a heterojunction to reduce the recombination rate. By preparing $SnO_x/ZnGa_2O_4$ heterojunction composite samples, Boppana *et al.* not only increased the formation rate of $^{\bullet}OH$ but also increased the photocatalytic degradation rate of cresol.[23] Chen *et al.* prepared one-dimensional $ZnGa_2O_4/ZnO$ nanowires by electrospinning method, and found that the nanowires are a new S-type heterojunction, which can achieve band bending by contacting the conduction band with weak reducing ability and the valence band with weak oxidizing ability, exposing the valence band with strong oxidizing ability and promoting electron transfer.[24] The ability to degrade TC-HCI was also improved. Therefore, for semiconductors with wide bandgap widths, heterojunction construction is often used as a standard method to accelerate electron–hole pair separation, in addition to precious metal deposition. When the band positions of the two semiconductors match each other, the corresponding bands undergo band bending, effectively separating the photogenerated electrons. Ga_2O_3 is an ultra-wide band gap semiconductor with a band gap of 4.4 eV, and its conduction position is even lower than that of $ZnGa_2O_4$, and its valence band position is slightly lower. Therefore, the suitable conduction and valence band positions of $ZnGa_2O_4$ are perfectly matched. Therefore, in this study, Ga_2O_3 and $ZnGa_2O_4$ were selected to form an S-type heterojunction to separate electron hole pairs and improve the photocatalytic performance.[25]

In addition, the photocatalytic performance of the two samples can be improved by constructing heterojunctions that accelerate the separation of the photogenerated carriers. The preparation of monomers with improved performance is also an efficient way to improve their performance. It was experimentally proved that the spherical shell structure can increase the specific surface area. Compared with the block or thin film structure, the smaller spherical shell structure not only increases the contact area with the solution but also reflects the incident light many times, which is another effective way to improve the photocatalytic performance.[26–29] The effective volume of the spherical shell structure is relatively large, which makes it easier to separate and deposit from the solution, and easy to recycle. There are many methods for preparing spherical shell structures, such as hydrothermal methods, anodic oxidation methods, electrodeposition methods, hard template methods and electrospinning methods.[30–32] Among them, the hydrothermal method has many advantages, such as simple operation, low cost, easy control of experimental conditions, high yield, shape can be controlled by conditions, *etc.*, and has attracted wide attention in recent years.[33,34]

In this study, $ZnGa_2O_4$ double-shell hollow spheres were prepared using a simple hydrothermal method. Ga_2O_3 quantum dots were grown on the surface of the shells, and their photocatalytic properties were investigated. The method used to prepare bishell $ZnGa_2O_4$ was based on a patent published by Zou Zhigang's team.[35] The difference is that the formation of bivalent $ZnGa_2O_4$ requires annealing, whereas hydrothermal GaOOH also requires annealing. Therefore, in this study, the precursors of the two materials were prepared using the hydrothermal method and then annealed uniformly. The results show that the $Ga_2O_3/ZnGa_2O_4$ heterojunction exhibits good photocatalytic performance, nearly 2 times that of the Ga_2O_3 monomer and nearly 3 times that of the $ZnGa_2O_4$ monomer.

2. Experiment

2.1 Materials

$Zn(NO_3)_2 \cdot 6H_2O$ from Damao and $Ga(NO_3)_3 \cdot xH_2O$ from Aladdin (99.99%) were used as the Zn and Ga sources in this study. The capture experiments of EDTA-2Na (99.0%), isopropyl alcohol (IPA) (99.7%) from Tianjin Damao Chemical Reagent Factory and ascorbic acid (VC) (99%) from Shanghai Aladdin Reagent Co., Ltd detected the key active substances in the photocatalytic process.

2.2 Synthesis

2.2.1 Preparation of the $ZnGa_2O_4$ template. $ZnGa_2O_4$, as an important part of an S-type heterojunction, has good morphology and a simple preparation method, which is particularly important to improve the performance. 1.19 g $Zn(NO_3)_2 \cdot 6H_2O$ and 3.07 g $Ga(NO_3)_3 \cdot xH_2O$ were dissolved in 50 mL ultra-pure water using the method of Zou Zhigang's team, and then fully stirred with 4 g citric acid; they were put into the inner tank of a hydrothermal kettle. The temperature was set at 200 °C and the reaction time was 10 h. The obtained precursor was HS-Z (hollow spheres $ZnGa_2O_4$). $ZnGa_2O_4$ double-shell hollow spheres can be prepared directly by annealing at 600 °C.

2.2.2 Preparation of Ga_2O_3 quantum dots. $GaCl_3$ and $C_{18}H_{15}N$ were mixed at a molar ratio of 1:1, dissolved in 40 mL DMF, and annealed after hydrothermal reaction to obtain Ga_2O_3 quantum dots.

2.2.3 Preparation of the $ZnGa_2O_4/Ga_2O_3$ heterojunction. Since both $ZnGa_2O_4$ and Ga_2O_3 need to be annealed, the precursor of Ga_2O_3 quantum dots can be obtained by hydrothermal growth on HS-Z after preparation. The specific steps are as follows:

(1) The precursor HS-Z obtained in 2.2.1, $GaCl_3$ and triphenylamine ($C_{18}H_{15}N$) were dissolved in 40 mL DMF in different proportions, as shown in Table 1, and stirred evenly. Since HS-Z was already obtained, it was only necessary to generate the precursor of Ga_2O_3 on its surface. Therefore, the hydrothermal temperature was set to 240 °C, and the hydrothermal time was set to 8 h. Note that the ratio given in the table is the ratio of $GaCl_3$ and HS-Z, and ZG0 is a $ZnGa_2O_4$ double-shell hollow

Table 1 Amounts of reagents used to prepare the samples

Sample name	Ratio	$GaCl_3$/mol	$C_{18}H_{15}N$/mol	HS-Z/mol
ZG0	0:1	0	0	0.003
ZG1	1:1	0.003	0.003	
ZG2	2:1	0.006	0.006	
ZG3	3:1	0.009	0.009	
ZG4	4:1	0.012	0.012	
GO	1:0	0.003	0.003	—

sphere obtained by direct annealing of HS-Z. There was no HS-Z in the GO sample; only Ga_2O_3 was prepared by $GaCl_3$ and $C_{18}H_{15}N$ feeding.

(2) After the hydrothermal reaction, the precipitate is centrifuged and dried. The product was heated at 2 °C min^{-1}, held for 2 h at 600 °C, and allowed to cool naturally. $ZnGa_2O_4/Ga_2O_3$ heterojunctions with different composite proportions were obtained.

2.3 Characterization

The samples were characterized by X-ray diffraction (XRD, DX-2700, Hao Yuan, China). The crystal phase of the sample was obtained using a Cu Kα radiation source with a radiation wavelength of 1.5406 A. The X-ray tube voltage was 40 kV, and the current was 30 mA. The morphology of the samples was measured by SEM (FEl Apreo S). TEM (FEI Tecnai G^2 F20) was used to observe the microstructure of the samples. The chemical states of each element in the sample were measured by X-ray photoelectron spectroscopy (XPS, Thermo Scientific, EscaLab Xi+), with Al Kα X-ray as the excitation source. Using Avantage software, the Powell algorithm and the Gauss-Lorentz fitting process (maximum iteration 100, convergence 0.0001) were used to obtain the experimental data. The UV-vis diffuse reflectance spectrum (UV-vis DRS) of the sample was obtained using $BaSO_4$ as the reference material. The measurement and analysis were performed by integrating a sphere (Hitachi, Japan) F-7000 ultraviolet-visible spectrophotometer.

2.4 Photocatalytic degradation test

To study the photocatalytic degradation of RhB dyes in the prepared samples. The photocatalytic experiment was carried out in a 50 mL RhB solution (10 mg L^{-1}) containing 10 mg of the photocatalyst. The light source used was a 500 W xenon lamp to simulate sunlight. First, the RhB solution containing the photocatalyst was stirred in the dark for 30 minutes to exclude the influence of the adsorption capacity of the photocatalyst on the experimental results. The RhB solution is then placed directly under the Xe lamp while keeping the distance between the light source and the solution constant. We placed 4 mL of each sample into a centrifuge tube every 10 minutes and centrifuged at 8000 RPM for 5 minutes to remove excess photocatalyst. To confirm each concentration of RhB, a UV-visible spectrophotometer (UV-vis abs, TU-1901) was used to analyze the absorption spectra of all solutions, with the wavelength range set to 400–700 nm.[36]

2.5 Experiment on the recovery cycle of the photocatalyst

Cyclic experiment is an important method to study the stability of photocatalysts. The detailed operations are described below. First, the rhodamine B solution after the first degradation is left to stand for a while so that the supernatant is separated from the lower catalyst, and the supernatant is slowly sucked out with a rubber head dropper, leaving the photocatalyst and a small part of the solution. Anhydrous ethanol was added to the solution containing the photocatalyst to promote the volatilization of the

solution, and the photocatalyst involved in the reaction was obtained for subsequent cyclic experiments.

2.6 Electrochemical test

The samples were analyzed at an electrochemical workstation with three electrodes. After weighing the 8 mg sample, 250 μL of ethanol and 750 μL of isopropyl alcohol were added, and ultrasonic dispersion was performed for 30 minutes, and 50 μL of Nafion perfluorinated resin solution was added, and ultrasound was continued for 30 minutes. The resulting suspension was slowly coated onto the surface of the glass carbon electrode using a pipette gun and allowed to naturally act as the working electrode. At the same time, 0.1 M L^{-1} Na_2SO_4 electrolyte solution 50 mL was prepared, and an Ag/AgCl electrode was used as the reference electrode. The electrolyte was analyzed by Mott–Schottky and electrochemical impedance spectroscopy (EIS). The Mott–Schottky test uses a platinum sheet as the counter electrode, and the EIS test uses a platinum wire as the counterelectrode.

3. Results and discussion

3.1 Morphology, phase, and composition characterization

The crystal structure of the prepared sample was determined by X-ray diffraction (XRD) experiment, and the results are shown in Fig. 1. Each sample has obvious diffraction peaks, which proves that the sample prepared by the hydrothermal experiment has high crystallinity. ZG0 conforms to the characteristic diffraction peaks in $ZnGa_2O_4$ (JCPDS#86-0412). GO conforms to the characteristic diffraction peak of α-Ga_2O_3 (JCPDS#006-0503). Interestingly, the characteristic peak of β-Ga_2O_3 appears in the standard diffraction peak of GO because GaOOH grows into α-Ga_2O_3 at low temperatures, and some of the α-Ga_2O_3 is converted to β-Ga_2O_3 at temperatures up to 600 °C. This result is consistent with those reported in other literature.[37,38] It is proved that sample ZG0 is $ZnGa_2O_4$ with lattice constants $a = b = c = 8.3352$ Å, $\alpha = \beta = \gamma = 90°$, and $a = b = 4.979$ Å, $c = 13.429$ Å, $\alpha = \beta = 90°$, $\gamma = 120°$. With the increase in $GaCl_3$ content during
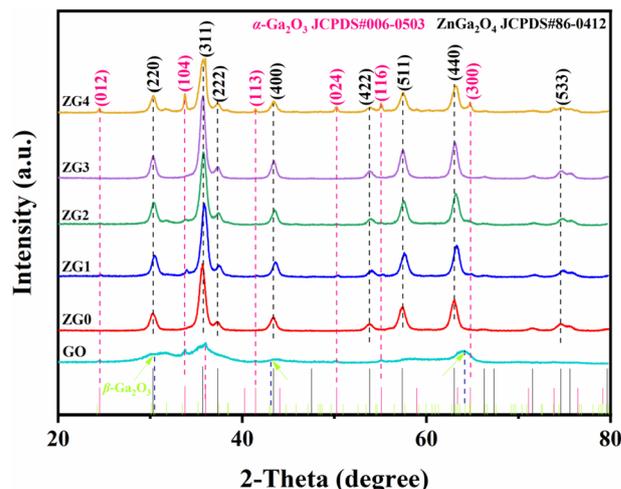

Fig. 1 XRD patterns of GO and ZG*X* samples (*X* = 0, 1, 2, 3, and 4).

the hydrothermal process, the characteristic diffraction peak of Ga_2O_3 was detected in the composite sample, *i.e.*, $ZnGa_2O_4$/Ga_2O_3 was formed. In addition, the characteristic peak response intensity of $ZnGa_2O_4$, which is mainly located at $2\theta = 35.697°$, gradually decreased, indicating that the content of $ZnGa_2O_4$ decreased. In addition to the characteristic peaks corresponding to the standard cards, no other diffraction peaks were detected, which shows that pure $ZnGa_2O_4$, Ga_2O_3 and $ZnGa_2O_4$/Ga_2O_3 were successfully prepared using the ratios shown in Table 1.

The scanning electron micrographs of the prepared samples are shown in Fig. 2. The GO sample presents an irregular agglomeration shape, and it was found that the sample presents a basic quantum dot shape with a size of about 10 nm after observation by transmission electron microscopy. In the HRTEM image, lattice streaks with lattice spacing of 2.55 Å can be observed, corresponding to the (111) crystal face of β-Ga_2O_3. Combined with XRD results, it is further demonstrated that the composite sample contains two crystal structures of α-Ga_2O_3 and β-Ga_2O_3, and the content of α-Ga_2O_3 is a little more. In Fig. 2(d)–(f), it can be seen that ZG0 presents a bishell spherical structure, and there is a certain gap between the inner sphere and the outer sphere, which is conducive to the extension and capture of the photon path in the photocatalytic reaction. It can be seen from TEM that the inner sphere of ZG0 and the outer sphere are different in light and dark, indicating that the inner sphere is not a hollow sphere, but a solid structure, and the outer sphere presents a hollow structure, and the overall structure is similar to the egg model. In Fig. 2(g)–(j), it can be seen that the composite sample as a whole presents a bivalve spherical structure similar to that of ZG0. After composite, the surface of the sample becomes rough, and the agglomeration

phenomenon occurs as GO quantum dots, indicating the successful preparation of the composite sample. In addition, the sizes of the composite samples did not show a particularly significant difference.

The surface chemical properties of the $ZnGa_2O_4$, Ga_2O_3 and $ZnGa_2O_4$/Ga_2O_3 composites were determined by X-ray photoelectron spectroscopy (Fig. 3). Fig. 3(a) shows the full spectrum of all samples in the binding energy range of 0–1350 eV. Peaks such as Ga 2p, Zn 2p, Ga LM2 and O 1s can be observed,[39] and characteristic signals of Zn can be observed in all samples except for Ga_2O_3. As can be seen from the diagram in Fig. 3(b), O 1s is divided into two different small peaks, where O_{II} corresponds to 532.4 eV, representing oxygen-containing compounds such as H_2O, O_2, or CO_2 adsorbed on the surface of the lattice and can be observed in all samples.[40] In GO, the O_I at 530.9 eV should be the result of the Ga–O bond,[41] which, along with XRD, can further determine that GO is pure Ga_2O_3. Compared with pure $ZnGa_2O_4$ (ZG0), the binding energy of the two peaks of lattice oxygen (O_I, O_{II}) in the composite sample is changed. The O_I position of ZG1 is lower than that of ZG0, and with an increase in the GO content, O_I and O_{II} move in a higher direction, indicating a change in the effect of metal ions on O atoms after heterojunction formation. Among the composite structures, ZG3 exhibited the highest O_I, indicating that ZG3 forms a relatively complete crystal structure with more Zn–O bonds. At the same time, the O_{II} area of the composite structure is increasing, indicating that the adsorption of oxygen-containing compounds on the surface of the sample is increasing, and more O_2 and CO_2 may be adsorbed on the surface. As shown in Fig. 3(c), Zn $2p^{1/2}$ and Zn $2p^{3/2}$ are divided into two peaks, respectively. The characteristic peaks of binding
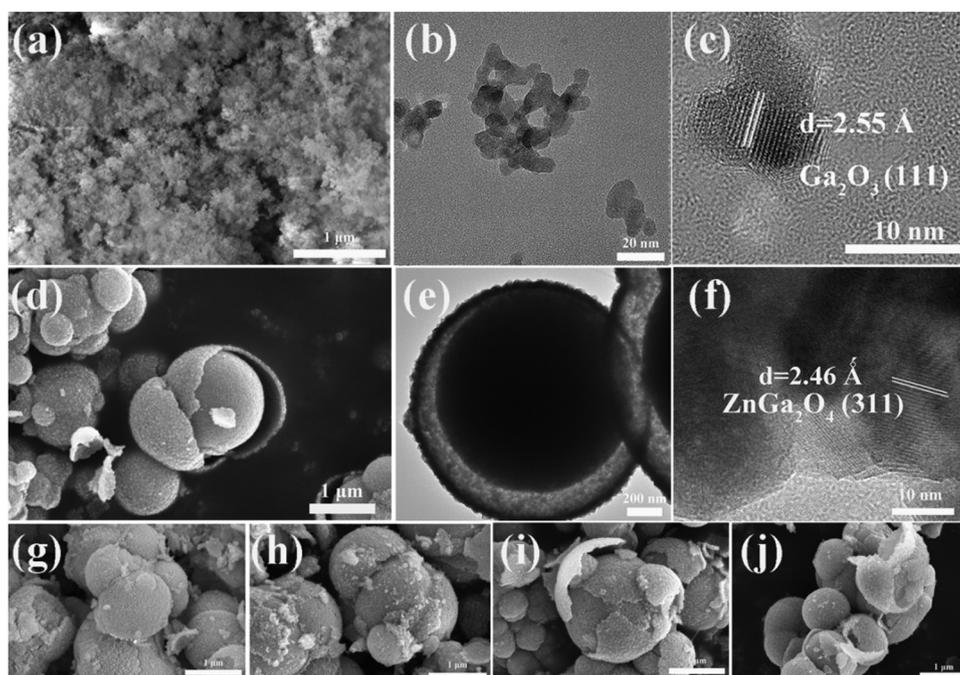

Fig. 2 SEM images of GO (a), ZG0 (d), ZG1 (g), ZG2 (h), ZG3 (i), ZG4 (j). TEM images and HRTEM images of GO (b) and (c) and ZG0 (e) and (f).
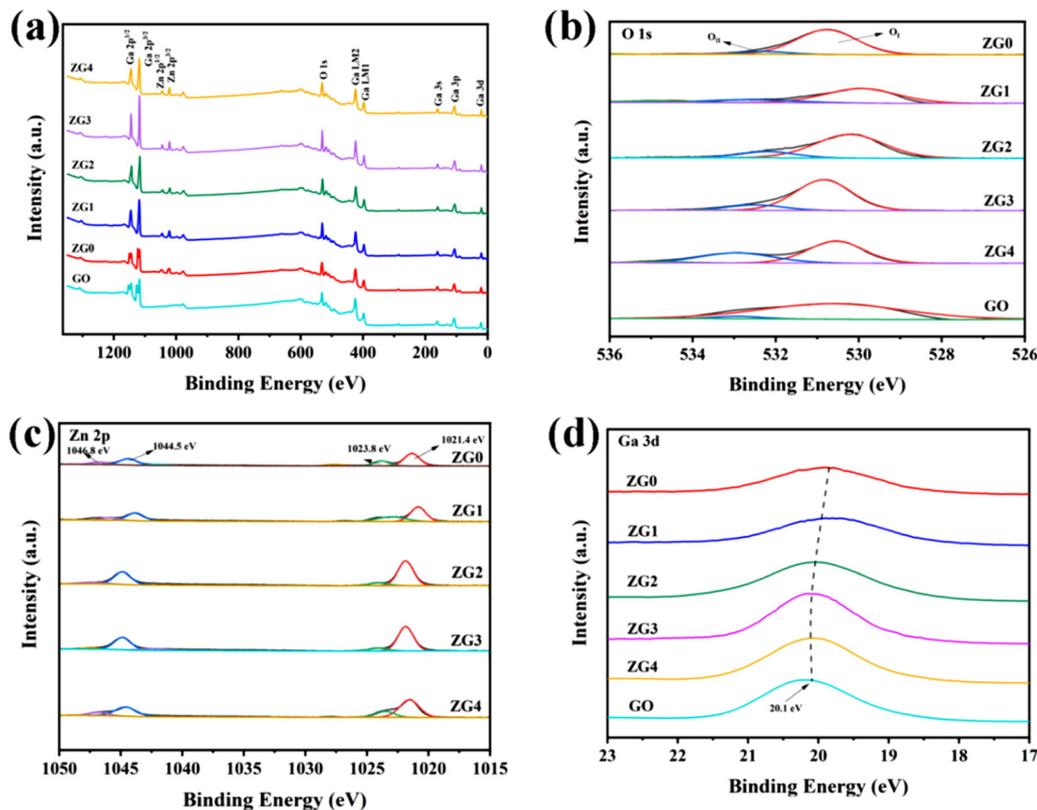
Fig. 3 (a) XPS full spectrum, (b) O 1s fine spectrum, (c) Zn 2p fine spectrum and (d) Ga 3d fine spectrum of all the samples.

energy at 1044.3 eV and 1021.4 eV indicate the presence of $ZnGa_2O_4$ in all samples, indicating the formation of the Zn–O bond. This confirms the successful preparation of $ZnGa_2O_4$/Ga_2O_3 heterojunctions. In addition, Fig. 3(d) shows the Ga 3d fine spectrum of all samples. With the increase in the GO content, the binding energy of the composite sample gradually approaches 20.1 eV, which further proves the existence of $ZnGa_2O_4$/Ga_2O_3 in the composite sample.

Fig. 4 shows the UV-vis DRS and Tauc of GO, ZG0, and ZG3. The absorption of ZG0 in the visible band (400–760 nm) is slightly higher than that of GO and ZG3, whereas the absorption in the

UVC band (200–280 nm) is significantly lower than that of GO and ZG3. For GO and ZG3, the sample has almost no light absorption in the visible band, and the light absorption of ZG3 in the UVC band is slightly higher than that of GO, which indicates that the composite sample can improve the light absorption of the sample in the deep ultraviolet band. Compared with ZG0, the light absorption of the composite sample in the visible band is reduced, which indicates that after the formation of the heterojunction, the oxygen vacancy of the composite sample is reduced, resulting in the reduction of defects and the increase of crystallinity, which is consistent with the XRD results.
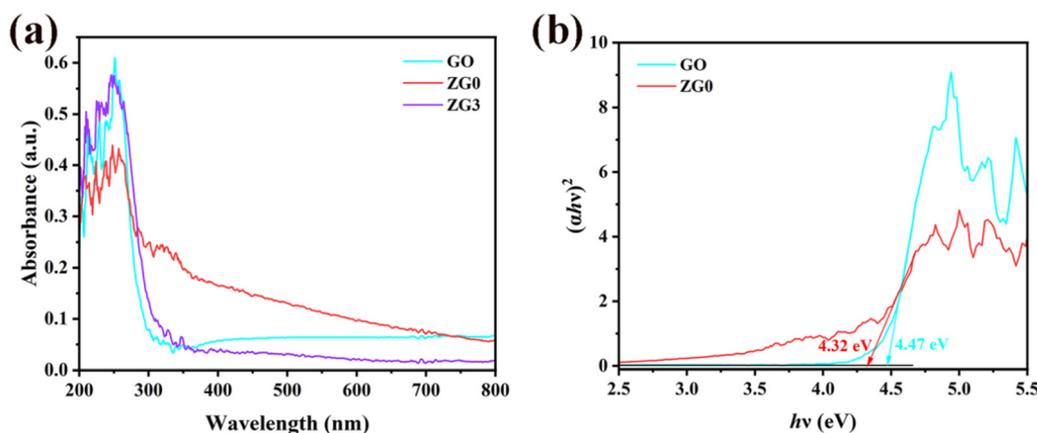

Fig. 4 UV-vis DRS (a) and corresponding Tauc plots (b) of GO, ZG0 and ZG3.

The experimental results show that the S-type heterojunction enhances the overall light absorption of the Ga$_2$O$_3$ and ZnGa$_2$O$_4$ monomers, thus improving their photocatalytic performance. Based on the UV-vis diffuse reflection absorption diagram (Fig. 4(b)), a Tauc diagram of the sample can be drawn. According to eqn (1), we obtain,

$$(\alpha h\nu)^{1/n} = C(h\nu - E_g) \tag{1}$$

In this formula, α is the absorption coefficient of the semiconductor, $h\nu$ is the energy of the incident light, and C is a constant. The type of semiconductor material determines the exponent n, where $n = 1/2$ when the semiconductor has a direct bandgap and $n = 2$ when the semiconductor has an indirect bandgap. ZnGa$_2$O$_4$ is a direct band gap semiconductor, so n is 1/2. According to the fitting calculation, it can be determined that the band gap width of ZG0 is 4.32 eV $\pm$ 0.01 eV and that of GO is 4.47 eV $\pm$ 0.01 eV, which is consistent with the literature report and further indicates that ZnGa$_2$O$_4$ is a wide band gap semiconductor material.[42–44]

3.2 Photocatalytic performance

To analyze the photocatalytic degradation efficiency of the prepared samples, a photocatalytic degradation experiment was conducted. Fig. 5(a) and (b) obtained by using the experimental method described in Section 2.4, are the photodegradation curves and the fitting graphs of the degradation efficiency of all samples. Where Dark is used to test the dark reaction adsorption capacity of the sample under dark conditions to achieve adsorption saturation of the sample without affecting the photoreaction degradation. After the dark reaction is complete, the organic solution is directly exposed to simulated sunlight. The horizontal axis represents the reaction time, and 0 indicates the end of the dark reaction and the beginning of the light reaction. C is the solution concentration after irradiation, and C_0 is the initial solution concentration.

Compared with the dark reaction, the degradation efficiency of RhB dyes by all heterojunction samples and monomers was significantly improved. It was also confirmed that the ZnGa$_2$O$_4$/Ga$_2$O$_3$ photocatalyst has certain photocatalytic potential for RhB dye reduction. The photocatalytic degradation efficiencies of ZG0 and GO for RhB dyes were 41.26% and 64.49%, respectively. Among the composite samples, ZG3 exhibited the best photocatalytic rate. After 20 min of irradiation with a 500 W xenon lamp, the photocatalytic degradation efficiency of ZG3 reached 95.21%. This result is due to the successful formation of the S-scheme heterojunction between ZG0 and GO, which reduces the recombination of electrons and holes and increases the number of active groups involved in the photocatalytic reaction. The Langmuir–Hinshelwood pseudo-first-order kinetic model (formula 2) was used to obtain the photocatalytic degradation rates of different samples, and the results are shown in Fig. 5(b). In formula (2), k is the first-order kinetic rate constant, and t is the illumination time. It is worth
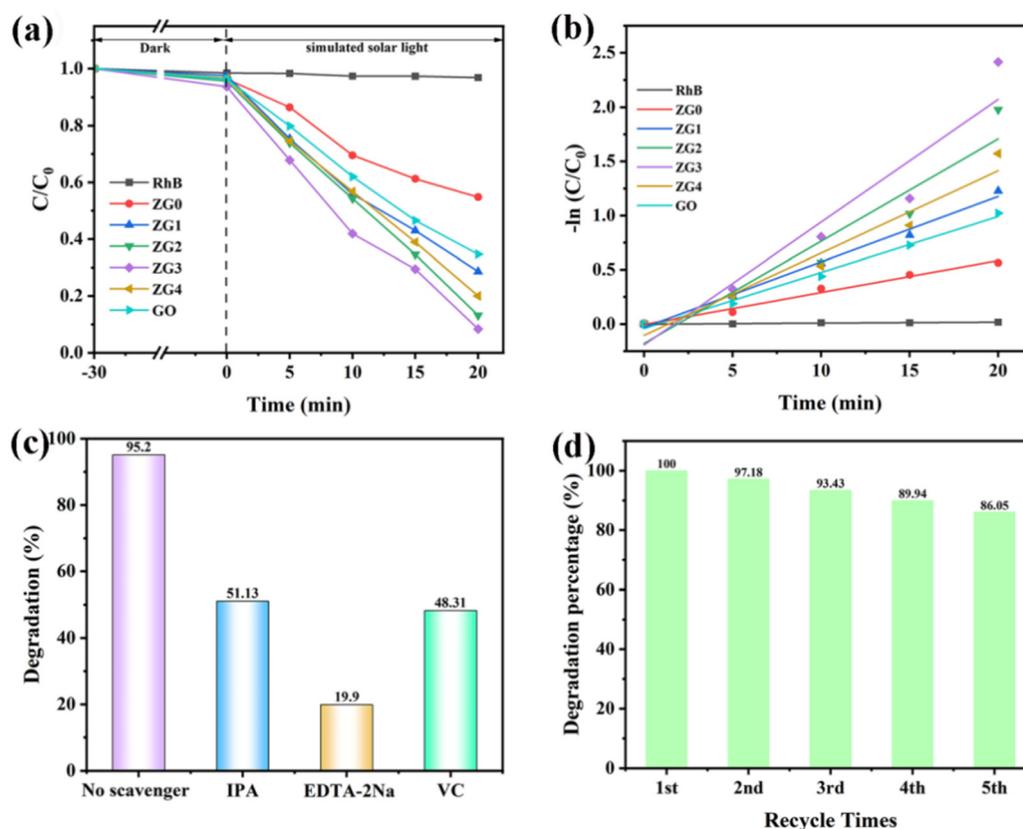

Fig. 5 Photocatalytic degradation diagram of all the samples (a), photocatalytic rate fitting diagram (b), capture experiment diagram of active substances during degradation process (c) and cycle experiment diagram of ZG3 (d).

mentioning that the self-degradation rate of RhB dye is 0.001 min^{-1}, which was almost negligible. In contrast, the photocatalytic degradation effects of ZG0 and GO on RhB dyes were significantly improved, which were 0.0297 min^{-1} and 0.0516 min^{-1}, respectively. The rate of composite samples was higher than the catalytic performance of each monomer. The fastest degradation rate of all samples was ZG3 (0.1133 min^{-1}), which was nearly 113 times faster than RhB dye. The results show that ZnGa$_2$O$_4$/Ga$_2$O$_3$ exhibits excellent recombination properties after forming a heterojunction.

$$-\ln\frac{C}{C_0} = kt \qquad (2)$$

The free radical trapping experiment is part of the research into photocatalytic degradation mechanisms. Isopropyl alcohol (IPA), EDTA-2Na and ascorbic acid (VC) can trap hydroxyl radical ($^{\bullet}$OH), hole (h$^+$) and superoxide radical ($^{\bullet}$O$_2^-$), respectively. As shown in Fig. 5(c), in the RhB dye degradation experiment with 10 mg ZG3 photocatalyst, the degradation rate reached 95.2% within 20 min before adding the collector and decreased to 51.13%, 19.9% and 48.31% after adding the collector, respectively. The photocatalytic degradation rate of ZG3 was inhibited to some extent by adding different types of trapping agents. In contrast, after adding EDTA-2Na, the photocatalytic degradation efficiency of ZG3 was significantly reduced, indicating that holes (h$^+$) played the largest role in the photocatalysis reaction.

To evaluate the chemical stability of ZG3, we conducted a cyclic experiment; the results are shown in Fig. 5(d). After 5 cycles, ZG3 can guarantee a degradation efficiency of close to 86% because ZnGa$_2$O$_4$ is a metal oxide of d^{10} configuration, belonging to the spinel type, which determines the excellent thermal and chemical stability of ZnGa$_2$O$_4$. The experimental results show that the catalyst exhibits good chemical stability and high recycling value.

3.3 Mechanism analysis

Fig. 6(a) shows the Mott–Schottky results for ZG0 and GO obtained from an electrochemical workstation. Using the Mott–Schottky equation (formula (3)), the relationship between the interface capacitance and the flat-band potential in the sample can be obtained.

$$\frac{1}{C^2} = \frac{2}{\varepsilon\varepsilon_0 e N_D}\left(V - V_{FB} - \frac{K_B T}{e}\right) \qquad (3)$$

Here, C is the interface capacitance, V_{FB} is the flat band potential, and V is the electrode potential. The Mott–Schottky curve can be obtained by plotting $1/C^2$ and V on the Y-axis and X-axis, respectively. The slope of the two curves in the figure is positive, indicating that ZG0 and GO are N-type semiconductors, and the formed heterojunction is an n–n type heterojunction. According to the image, the V_{FB} of ZG0 and GO are -0.89 V and -1.25 V, respectively. For N-type semiconductors, V_{FB} typically has a positive conduction potential (E_{CB}) of 0.1–0.3 V, and for P-type semiconductors, V_{FB} has a negative valence band potential (E_{CB}) of 0.1–0.3 V.[45–49] Based on the experimental results, it can be inferred that the E_{CB} of ZG0 and GO are -0.99 V and -1.35 V (vs. Ag/AgCl); thus, the E_{CB} for ZG0 and GO are -0.79 and -1.15 eV, respectively. The XPS band spectra can be used to approximate the top positions of ZnGa$_2$O$_4$ and Ga$_2$O$_3$. Fig. 6(b) shows the XPS band spectra. According to the images, the highest position of the ZnGa$_2$O$_4$ band was 2.95 eV, while the highest position of the Ga$_2$O$_3$ band top was 3.07 eV. Combining the results of the Mott–Schottky test with the results of the Tauc diagram in Fig. 4(b), two semiconductor valence band positions can be deduced according to the formula (eqn (4)), the ZnGa$_2$O$_4$ valence band is 3.53 eV, and the Ga$_2$O$_3$ valence band is 3.32 eV.

$$E_{VB} = E_{CB} + E_g \qquad (4)$$

To further explain the reason for the improvement of the photocatalytic performance after heterojunction formation, the charge transfer characteristics of the GO, ZG0 and ZG3 samples were studied by electrochemical impedance tests, as shown in Fig. 7. The EIS Nyquist arc of ZG3 is smaller than that of GO and ZG0, indicating that electron transfer is easier at the ZG3 interface than at the GO and ZG0 interfaces. At the same time, ZG3 exhibits low charge transfer resistance, further indicating that the formation of S-type heterojunctions can reduce the
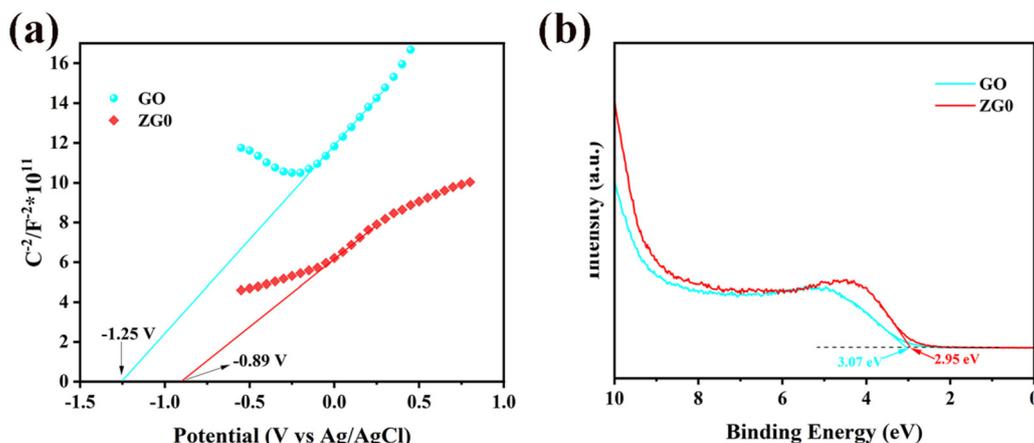

Fig. 6 Mott–Schottky plot (a) and XPS valence band spectra (b) of ZG0 and GO at an excitation wavelength of 263 nm.
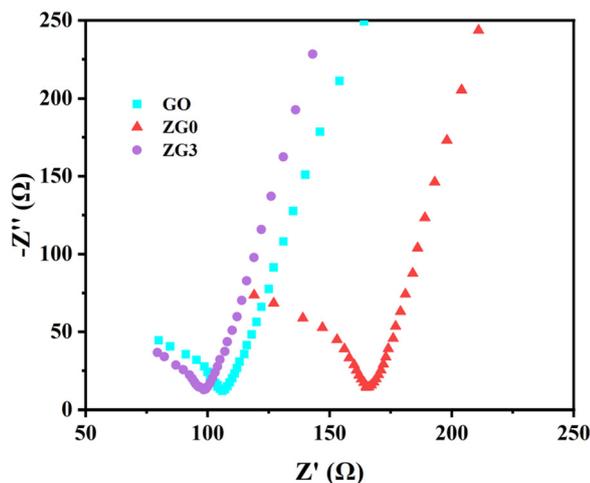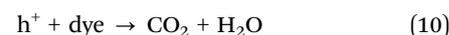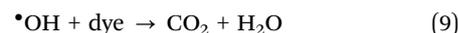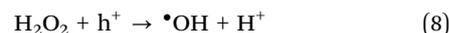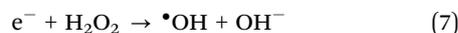
Fig. 7 EIS images of GO, ZG0, and ZG3.

diffusion resistance and effectively inhibit the photogenerated carrier recombination, thus enhancing the charge transfer ability and improving the photocatalytic performance of the composite.

In summary, the band structure diagram shown in Fig. 8 can be obtained. Before the contact between the two semiconductors, the E_f of ZnGa$_2$O$_4$ was 2.95 eV higher than that of VB, and the E_f of Ga$_2$O$_3$ was 3.07 eV higher than that of VB. The specific values in Fig. 8 can be obtained from the previous experiments. The results obtained before and after the two semiconductor contacts are shown in Fig. 8. Due to the different positions of the Fermi levels in ZnGa$_2$O$_4$ and Ga$_2$O$_3$, an internal electric field is formed at the contact interface. The electrons in the CB of ZnGa$_2$O$_4$ spontaneously recombine with the holes in the VB of Ga$_2$O$_3$ to balance the energy level difference caused by the Fermi level; band bending occurs, and an S-type heterojunction is formed, thus accelerating the separation of electrons and holes. At the same time, h$^+$ in the VB containing ZnGa$_2$O$_4$ and e$^-$ in the CB containing Ga$_2$O$_3$ participate in the photocatalytic

reaction to form the reaction groups $^\bullet$OH, $^\bullet$O$_2^-$ and h$^+$. The main reaction modes of the different reaction groups are shown in eqn (5)–(10). In addition, the reactive group that affects the photocatalytic reaction is h$^+$.

$$O_2 + e^- \rightarrow {}^\bullet O_2^- \tag{5}$$

$${}^\bullet O_2^- + 2H^+ + e^- \rightarrow H_2O_2 \tag{6}$$

$$e^- + H_2O_2 \rightarrow {}^\bullet OH + OH^- \tag{7}$$

$$H_2O_2 + h^+ \rightarrow {}^\bullet OH + H^+ \tag{8}$$

$${}^\bullet OH + dye \rightarrow CO_2 + H_2O \tag{9}$$

$$h^+ + dye \rightarrow CO_2 + H_2O \tag{10}$$

4. Conclusion

In summary, we successfully prepared bishell hollow spherical ZnGa$_2$O$_4$, Ga$_2$O$_3$ quantum dots and S-type heterojunction ZnGa$_2$O$_4$/Ga$_2$O$_3$ hollow spherical photocatalysts by a one-step hydrothermal method, all of which exhibited good photocatalytic properties for RhB dye. The degradation efficiency of ZnGa$_2$O$_4$ and Ga$_2$O$_3$ reached 41.26% and 64.49%, respectively, after 20 min of irradiation by a 500 W xenon lamp. In addition, the ZnGa$_2$O$_4$/Ga$_2$O$_3$ heterojunctions exhibited better photocatalytic performance than the conventional ones. Under the same conditions, the degradation efficiency of the ZnGa$_2$O$_4$/Ga$_2$O$_3$ heterojunction prepared at a feed ratio of 1:3 was 95.21%. In addition, the capture experiment it is proven that the active substance that plays a key role in catalysis is h$^+$. The S-type heterojunction can recombine electrons and holes with weak reducing and oxidizing ability and expose electrons holes with strong REDOX ability, thus significantly improving the photocatalytic performance. This study provides a new and convenient method for the simple and efficient preparation of bishell hollow spheres ZnGa$_2$O$_4$/Ga$_2$O$_3$ and a new idea for the

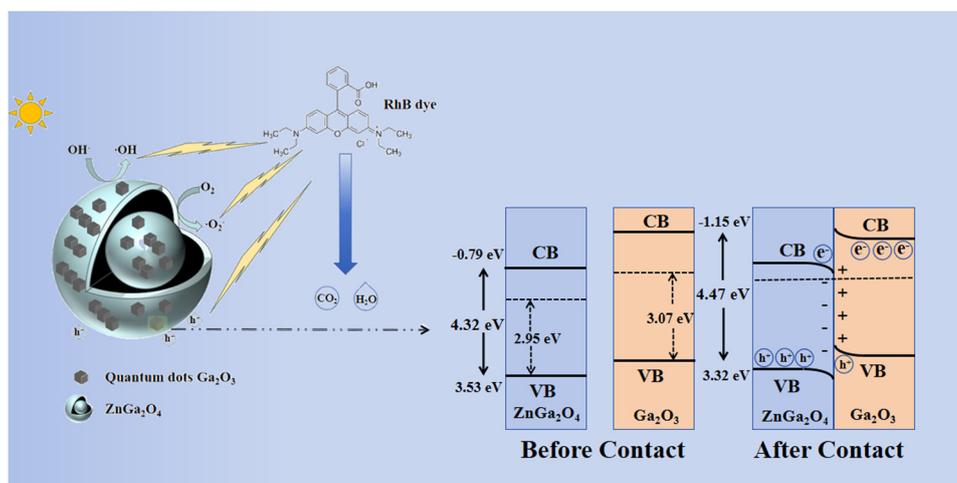**Fig. 8** Schematic of the ZnGa$_2$O$_4$/Ga$_2$O$_3$ before contact and illustration of the photocatalytic mechanism in the S-scheme heterojunction.

degradation of organic pollutants such as RhB. The synthesized $ZnGa_2O_4/Ga_2O_3$ has potential application prospects in other environmental treatment fields.

Author contributions

Zeyu Yang: conceptualization, methodology, data curation, writing – original draft. Jizhou Yang: conceptualization, methodology, data curation, writing – original draft. Haibo Fan: conceptualization, methodology, data curation, writing – review and editing.

Data availability

All data generated and/or analysed during this study are included in this published article and its ESI.†

Conflicts of interest

The authors declare no competing financial interest.

Acknowledgements

References

1 E. Hu, X. Wu, S. Shang, X. M. Tao, S. X. Jiang and L. Gan, Catalytic ozonation of simulated textile dyeing wastewater using mesoporous carbon aerogel supported copper oxide catalyst, *J. Cleaner Prod.*, 2016, **112**, 4710–4718.

2 J. S. Dalton, P. A. Janes, N. G. Jones, J. A. Nicholson, K. R. Hallam and G. C. Allen, Photocatalytic oxidation of NO_x gases using TiO_2: a surface spectroscopic approach, *Environ. Pollut.*, 2002, **102**, 415–422.

3 D. Rajkumar and J. G. Kim, Oxidation of Various Reactive Dyes With *In Situ* Electrogenerated Active Chlorine for Textile Dyeing Industry Wastewater Treatment, *J. Hazard. Mater.*, 2006, **136**, 203–212.

4 A. Mills, C. O'Rourke, V. Kalousek and J. Rathousky, Adsorption and photocatalytic and photosensitised bleaching of acid orange 7 on multilayer mesoporous films of TiO_2, *J. Hazard. Mater.*, 2003, **99**, 182–187.

5 Y. Wang, C. Zhang, J. Sun and Z. Zhang, Adsorption behavior of methyl orange onto nanoporous core–shell $Cu@Cu_2O$ nanocomposite, *Chem. Eng. J.*, 2013, **10**, 24–32.

6 M. X. Huo, Y. L. Jin, Z. F. Sun, F. Ren, L. Pei and P. G. Ren, Facile synthesis of chitosan-based acid-resistant composite films for efficient selective adsorption properties towards anionic dyes, *Carbohydr. Polym.*, 2021, **254**, 117473.

7 J. A. Laszlo, Regeneration of Azo-Dye-Saturated Cellulosic Anion Exchange Resin by Burkholderia cepacia Anaerobic Dye Reduction, *Environ. Sci. Technol.*, 2000, **34**.

8 M. A. Rauf and S. S. Ashraf, Survey of recent trends in biochemically assisted degradation of dyes, *Chem. Eng. J.*, 2012, **209**, 520–530.

9 M. R. Hoffmann, S. T. Martin, W. Choi and D. W. Bahnemann, Environmental Applications of Semiconductor Photocatalysis, *Chem. Rev.*, 1995, **95**, 69–96.

10 H. Kisch, Semiconductor Photocatalysis—Mechanistic and Synthetic Aspects, *Angew. Chem., Int. Ed.*, 2013, **52**, 812–847.

11 A. Mills, R. H. Davies and D. Worsley, Water purification by semiconductor photocatalysis, *Chem. Soc. Rev.*, 1993, **22**, 417–425.

12 A. Mills, R. H. Davies and D. Worsley, ChemInform Abstract: Water Purification by Semiconductor Photocatalysis, *Cheminform*, 1993, **22**, 417–425.

13 R. Abe, K. Sayama and H. Arakawa, Significant influence of solvent on hydrogen production from aqueous I 3/I redox solution using dye-sensitized Pt/TiO_2 photocatalyst under visible light irradiation, *Chem. Phys. Lett.*, 2003, **379**, 230–235.

14 Q. Wu, J. Ouyang, K. Xie, L. Sun, M. Wang and C. Lin, Ultrasound-assisted synthesis and visible-light-driven photocatalytic activity of Fe-incorporated TiO_2 nanotube array photocatalysts, *J. Hazard. Mater.*, 2012, **199**, 410–417.

15 H. Y. Yang, S. F. Yu, S. P. Lau, X. Zhang and G. Jun, Direct Growth of ZnO Nanocrystals onto the Surface of Porous TiO_2 Nanotube Arrays for Highly Efficient and Recyclable Photocatalysts, *Small*, 2010, **5**, 2260–2264.

16 Y. Hou, W. Wang, L. Wu, Z. Ding and X. Fu, Efficient decomposition of benzene over a beta-Ga_2O_3 photocatalyst under ambient conditions, *Environ. Sci. Technol.*, 2006, **40**, 5799.

17 V. R. Choudhary, S. K. Jana and B. P. Kiran, Highly active Si-MCM-41-supported Ga_2O_3 and In_2O_3 catalysts for Friedel-Crafts-type benzylation and acylation reactions in the presence or absence of moisture – ScienceDirect, *J. Catal.*, 2000, **192**, 257–261.

18 W. Xiang, X. Qian, L. Mingrun, S. Shuai, W. Xiuli, W. Yaochuan, F. Zhaochi, S. Jingying, H. Hongxian and L. Can, Photocatalytic overall water splitting promoted by an α-β phase junction on Ga_2O_3, *Angew. Chem., Int. Ed.*, 2012, **51**(52), 3089–3092.

19 M. Chen, A. K. Singh, J. L. Chiang, R. H. Horng and D. S. Wuu, Zinc Gallium Oxide – Review from Synthesis to Applications, *Nanomaterials*, 2020, **10**, 2208.

20 M. Sun, D. Li, W. Zhang, Z. Chen and X. Fu, ChemInform Abstract: Rapid Microwave Hydrothermal Synthesis of $ZnGa_2O_4$ with High Photocatalytic Activity Toward Aromatic Compounds in Air and Dyes in Liquid Water, *J. Solid State Chem.*, 2012, **190**, 135–142.

21 Y. Inoue, Photocatalytic water splitting by RuO_2-loaded metal oxides and nitrides with d^0- and d^{10}-related electronic configurations, *Energy Environ. Sci.*, 2009, **2**, 364–386.

22 A. Ghaffar, L. Zhang, X. Zhu and B. Chen, Porous PVdF/GO Nanofibrous Membranes for Selective Separation and Recycling of Charged Organic Dyes from Water, *Environ. Sci. Technol.*, 2018, **52**, 4265–4274.

23 V. B. R. Boppana and R. F. Lobo, SnO$_x$–ZnGa$_2$O$_4$ Photocatalysts with Enhanced Visible Light Activity, *ACS Catal.*, 2011, **1**, 923–928.

24 W. Chen, T. Kang, F. Du, P. Han, M. Gao, P. Hu, F. Teng and H. Fan, A new S-scheme heterojunction of 1D ZnGa$_2$O$_4$/ZnO nanofiber for efficient photocatalytic degradation of TC-HCl, *Environ. Res.*, 2023, **232**, 116388.

25 A. C. Draa, F. Mokhtari, I. Lasloudji, S. Zermout and K. Lebbou, Internal radiation effect on semiconductor β-Ga$_2$O$_3$ crystals grown by the VB Method and anisotropic thermal stress, *J. Cryst. Growth*, 2024, 648.

26 K. J. C. V. Bommel, A. Friggeri and S. Shinkai, Organic Templates for the Generation of Inorganic Materials, *Chem. Inf.*, 2003, **34**, 980–999.

27 F. Caruso, R. A. Caruso and H. Moehwald, Nanoengineering of Inorganic and Hybrid Hollow Spheres by Colloidal Templating, *Science*, 1998, **282**, 1111–1114.

28 J. Yang, T. Kang, P. Han, W. Chen, Z. Chen, Z. Wan, Z. Liu, F. Teng, P. Hu and H. Fan, Enhanced photocatalytic performance of Ga$_2$O$_3$ hollow spheres prepared by hard template technique, *Mater. Sci. Semicond. Process.*, 2024, **178**, 108466.

29 Z. Y. Zhong, Y. D. Yin, B. Gates and Y. N. Xia, Preparation of Mesoscale Hollow Spheres of TiO$_2$ and SnO$_2$ by Templating Against Crystalline Arrays of Polystyrene Beads, *Adv. Mater.*, 2000, **12**, 206–209.

30 H. Xu and W. Wang, Template Synthesis of Multishelled Cu$_2$O Hollow Spheres with a Single-Crystalline Shell Wall, *Angew. Chem., Int. Ed.*, 2007, 1489–1492.

31 X. Li, Y. Xiong, Z. Li and Y. Xie, Large-scale fabrication of TiO$_2$ hierarchical hollow spheres, *Inorg. Chem.*, 2006, **45**, 3493–3495.

32 J. Yu and X. Yu, Hydrothermal Synthesis and Photocatalytic Activity of Zinc Oxide Hollow Spheres, *Environ. Sci. Technol.*, 2008, **42**, 4902.

33 X. Bu, P. Feng, T. E. Gier, D. Zhao and G. D. Stucky, Hydrothermal Synthesis and Structural Characterization of Zeolite-like Structures Based on Gallium and Aluminum Germanates, *J. Am. Chem. Soc.*, 1999, **120**, 735–741.

34 J. W. Hedenquist and J. B. Lowenstern, The role of magmas in the formation of hydrothermal ore deposits, *Nature*, 1994, **370**, 519–527.

35 Z. Yong, Z. Yuan and Z. Zhigang, Preparation method of ZnGa$_2$O$_4$ double-shell hollow nanospheres, 2017.

36 V. Wenckstern, Holger, Group-III Sesquioxides: Growth, Physical Properties and Devices, *Adv. Electron. Mater.*, 2017, 1600350.

37 H. S. Qian, P. Gunawan, Y. X. Zhang, G. F. Lin and R. Xu, Template-Free Synthesis of Highly Uniform α-GaOOH Spindles and Conversion to α-Ga$_2$O$_3$ and β-Ga$_2$O$_3$, *Cryst. Growth Des.*, 2009, **8**, 1282–1287.

38 Y. Quan, S.-Q. Liu, K.-L. Huang, D. Fang, X.-Y. Zhang and H.-W. Hou, Hydrothermal synthesis and characterization of Eu-doped GaOOH/α-Ga$_2$O$_3$/β-Ga$_2$O$_3$ nanoparticles, *Trans. Nonferrous Met. Soc. China*, 2010, 1458–1462.

39 A. K. Singh, C.-C. Yen, K.-P. Chang and D.-S. Wuu, Influence of Al doping on crystal structure, optical, and photoluminescence characteristics of ZnGa$_2$O$_4$ films, *Mater. Sci. Semicond. Process.*, 2022, 106962.

40 F. Du, D. Sun, Y. Jiao, Y. Teng, F. Fan and F. Haibo, Electrospun Zn-doped Ga$_2$O$_3$ nanofibers and their application in photodegrading rhodamine B dye, *Ceram. Int.*, 2021, **47**, 4963–4971.

41 J. Tao, H. L. Lu, Y. Gu, H. P. Ma, X. Li, J. X. Chen, W. J. Liu, H. Zhang and J. J. Feng, Investigation of growth characteristics, compositions, and properties of atomic layer deposited amorphous Zn-doped Ga$_2$O$_3$ films, *Appl. Surf. Sci.*, 2019, **476**, 733–740.

42 M. G. Brik, A. M. Srivastava and A. I. Popov, A few common misconceptions in the interpretation of experimental spectroscopic data, *Opt. Mater.*, 2022, **127**, 112276.

43 H. Dixit, N. Tandon, S. Cottenier and M. Waroquier, *Electronic structure and band gap of zinc spinel oxides beyond LDA: ZnAl$_2$O$_4$, ZnGa$_2$O$_4$ and ZnIn$_2$O$_4$,* IOP Publishing, 2011.

44 H. L. Lu, Y. Gu, H. P. Ma, X. Li, J. X. Chen, W. J. Liu, H. Zhang and J. J. Feng, Investigation of growth characteristics, compositions, and properties of atomic layer deposited amorphous Zn-doped Ga$_2$O$_3$ films, *Appl. Surf. Sci.*, 2019, **476**, 733–740.

45 F. Guo, W. Shi, H. Wang, M. Han, H. Li, H. Huang, Y. Liu and Z. Kang, Facile fabrication of a CoO/g-C$_3$N$_4$ p–n heterojunction with enhanced photocatalytic activity and stability for tetracycline degradation under visible light, *Catal. Sci. Technol.*, 2017, **7**, 3325–3331.

46 B. A. Pinaud, Z. Chen, D. N. Abram and T. F. Jaramillo, Thin Films of Sodium Birnessite-Type MnO$_2$: Optical Properties, Electronic Band Structure, and Solar Photoelectrochemistry, *J. Phys. Chem. C*, 2011, **115**, 11830–11838.

47 S. I. Stepanov, V. I. Nikolaev, V. E. Bougrov and A. E. Romanov, Gallium oxide: Properties and applications – A review, *Rev. Adv. Mater. Sci.*, 2016, **44**, 63–86.

48 Z. P. Ma, L. Zhang, X. Ma and F. N. Shi, A dual strategy for synthesizing crystal plane/defect co-modified BiOCl microsphere and photodegradation mechanism insights, *J. Colloid Interface Sci.*, 2022, 73–83.

49 J. Zheng and Z. Lei, *Incorporation of CoO nanoparticles in 3D marigold flower-like hierarchical architecture MnCo$_2$O$_4$ for highly boosting solar light photo-oxidation and reduction ability,* Elsevier, 2018.